Attenuation compensation for georadar data by Gabor deconvolution

Robert J. Ferguson and Gary F. Margrave

ABSTRACT

It has been shown through previous data examples that nonstationary deconvolution, and in particular the CREWES Gabor nonstationary deconvolution, provides significant enhancement for deep georadar reflections. In many examples the improvement extends the radar image from a few meters to a few tens of meters.

We find here through controlled experiment that nonstationary deconvolution has an attenuation correction property - the frequency and phase components of attenuation loss are compensated for. Though the compensation effect is noticeable on seismic data, the effect on georadar data is quite a bit more obvious and we find that, in terms of attenuation factor Q, Q is about an order of magnitude smaller (so the attenuation effect is much larger) for georadar than it is for seismic. We show that it this Q compensation probably accounts for the significant signal improvements that we see in georadar data.

INTRODUCTION

Recent application of the CREWES Gabor nonstationary deconvolution algorithm (Gabor decon, Margrave et al. (2011)) to georadar data has lead to significant improvements in depth of image penetration. For example, in Ferguson et al. (2011) increase the image from meters to ten meters in a quarry. Ferguson et al. (2010) and Rowell et al. (2010) extend the image in basalt to 35 meters. In each of Ferguson et al. (2011), Ferguson et al. (2010), and Rowell et al. (2010), data acquisition time (the number of sample acquired) appears to be the limiting factor in image depth when Gabor decon is used.

More recently Ferguson et al. (2012b) provide images tens of meters below a nuclear weapons repository in the French Alps, and Ferguson et al. (2012a) triple the effective time length of their data with Gabor decon.

We postulate that Gabor decon has significant Q compensation attributes and so it will return very good results for signals like georadar that have weak Q values. We then estimate Q for a recent georadar acquisition in the Alps of Central Italy. We find that the extracted value $(Q = 21.8)$ is about 10 times smaller than what is typical of seismic data $(Q \sim 10^2)$. We then generate two synthetic signals - a georadargram and a seismogram - for the same reflectivity sequence and we scale these by a georadar wavelet of 200 MHz central frequency and a seismic wavelet of 20 Hz respectively. The georadargram is then attenuated using $Q = 21.8$ and the seismogram is attenuated using $Q = 218$, and then they are both input to Gabor deconvolution. We find that the georadar signal is significantly attenuated in amplitude and that reflections appear to be shifted to earlier times. In contrast, the seismic signal is much less attenuated and reflections are not as severely time shifted.

As expected, Gabor decon does an excellent job of restoring the amplitude and phase characteristics of the seismogram, but that the phase characteristics of the georadargram do

remain shifted though they are improved. We conclude that previous findings that Gabor decon drastically improves georadar images is most probably due to Q compensation.

THEORY

Gabor deconvolution

Gabor decon is based on Margrave et al. (2011) and we will review it's most salient points here. This nonstationary deconvolution algorithm is based on assumptions of white reflectivity and minimum-phase source wavelet similar to Weiner deconvolution (Robinson, 1967). The data model upon which Margrave et al. (2011) is based is that the Gabor transform of a trace is approximately equal to the Gabor transforms of reflectivity, the source wavelet, and the attenuation mechanism multiplied together. Margrave et al. (2011) compute the Gabor spectrum of estimated reflectivity through division of the spectrum of the trace by the spectrum of the combined estimate of the wavelet / attenuation function.

The deconvolution operator is determined from the data directly, so attenuation that is removed is consistent with the data such that the deconvolution process is stable Margrave et al. (2011). The source wavelet w and the attenuation function α are treated as separate, convolutional (in time) effects where the wavelet is assumed to be stationary, and all nonstationary effects are due to attenuation Margrave et al. (2011). Attenuation includes constant Q that causes frequency-dependent loss of amplitude and the short-path multiple effect of O'Doherty and Anstey (1971); they combine to form an effective attenuation mechanism with the frequency dependent and minimum phase characteristics.

In the Gabor domain of time t and frequency f, the model of an attenuated seismic trace is

$$\hat{S}_g\left(t,f\right) \approx \hat{w}\left(f\right)\, \alpha\left(t,f\right)\, \hat{r}_g\left(t,f\right), \tag{1}$$

where

$$\hat{r}_g\left(t_k,f\right) = \int_{-\infty}^{\infty} g_k\left(t\right)\, r\left(t\right)\, e^{-2\,\pi\, i\, f\, t}\, dt \tag{2}$$

is the Gabor transform of time-domain reflectivity r, and g is a partition of unity (POU). Variables t_k and f are the two coordinates of the Gabor domain (Gabor time and Gabor frequency).*

A POU is a set of localizing windows within which the propagating wavefield is assumed to be stationary and who's superposition sums to unity Margrave et al. (2011). Figure 1 demonstrates this property. In Figure 1(a), 20 overlapping Gaussians are plotted on a time axis between 0 and 3 μs - they are identical except for a time shift. Figure 1(b) shows a plot of the sum of the amplitudes of the 20 Gaussians in 1(a). The triangles annotated on the resulting curve indicate the range of complete overlap of the Gaussians, and within this range, the sum is identically unity. Any process that is applied in the Gabor domain, then, will be correct only within this range. An example of the application of a POU to a

*The Gabor time coordinate t_k is given as t_k in Margrave et al. (2011). We use the subscript g here rather than k to reduce confusion between the discrete number of windows $1 \leq k \leq M$ and the discrete number of Gabor time samples $1 \leq g \leq N$.

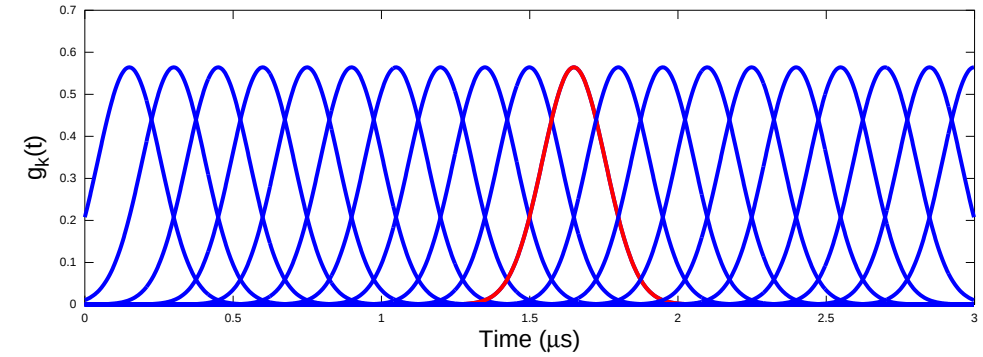

(a)

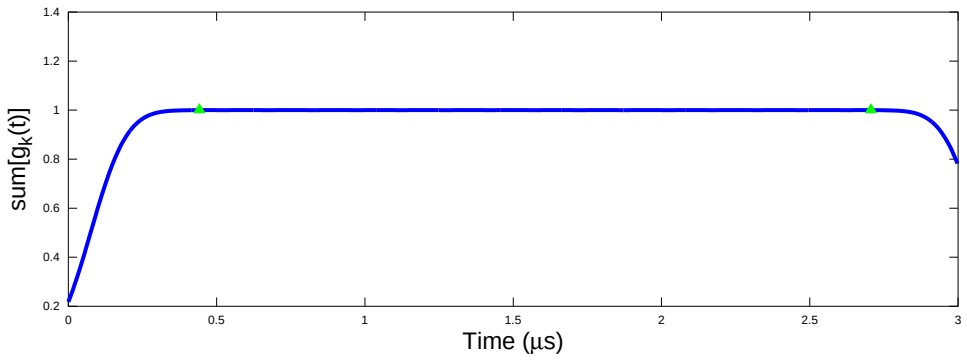

(b)

FIG. 1. Example of a partition of unity (POU). a) 20 identical Gaussian windows shifted by a constant increment. b) The sum of the Gaussian windows in (a). The sum is identically unity within the time range indicated by the triangles on (b).

time-domain reflectivity series is given in Figure 2. A reflectivity time-series r is plotted in Figure 2(a) and the Gaussian $g_{k=11}$ that is highlighted on Figure 1 is plotted for reference. Figure 2(b) is a plot of $g_{11}\, r$ - reflections outside the range of g_{11} are zeroed, and reflections within g_{11} are scaled according to the shape of g_{11}. Plotted in Figure 2(c) is the reconstruction of r as a sum of the 20 windowed reflectivities $\sum_k g_k\, r^{\dagger}$. Within the exact range (indicated by the triangles) reflectivity r is precisely recovered while outside of this range (in particular between 0 and 5 μs) reflections are reduced in amplitude. To arrive at this practical solution for $\hat{r}_g$ (equation 2), a number of assumptions are made and these are: a) the attenuation function α varies slowly with respect to the POU, b) the time-domain convolution of the wavelet with the attenuation function decays rapidly away from $t = 0$ (is centred on $t = 0$) due to w being short in time relative to the POU, and c) reflectivity r is windowed twice - once by the analysis window and again by the synthesis window, so the combined effects of the two windows on r is to pass small values except where the windows overlap Margrave et al. (2011).

Deconvolution then proceeds as a solution for $\hat{r}_g using$ equation 1:

$$\hat{r}_g\,(t,f) \approx \hat{S}_g\,(t,f) \div [\hat{w}\,(f)\;\alpha\,(t,f)]\,, \tag{3}$$

(Margrave et al., 2011) followed by an inverse Gabor transform according to

$$r\,(t) \approx \sum_k g_k\,(t_k)\,\mathrm{IFT}_{f\to t}\left\{\hat{r}_g\,(t_k,f)\right\}, \tag{4}$$

where $\mathrm{IFT}_{f\to t}$ indicates the $f \to t$ inverse Fourier transform (Margrave et al., 2011). Estimation of $\hat{w}\,\alpha$ is done using either boxcar smoothing of $\hat{S}_g$ or, more commonly, hyperbolic smoothing of $\hat{S}_g$ (Margrave et al., 2011) analogous to the wavelet prediction method of Robinson (1967) in that the Hilbert transform is used to relate the amplitude and phase of w.

Q estimation by the spectral-ratio method

Most media attenuate individual frequencies of a propagating wavefield (Zener, 1948). Q is a common measure of this attenuation, and it is usually defined in terms of peak strain-energy E and energy loss per period ΔE according to (Zener, 1948):

$$Q\,(f) = -\frac{2\,\pi\,E_f}{\Delta E_f}. \tag{5}$$

Because Q estimates are often stationary in f they can be estimated in the frequency domain through fitting a slope to the amplitude spectrum - the *spectral ratio method* (Båth, 1974). Two different measurements of the source waveform for two different receivers are obtained and Q is estimated by slope fitting along the f coordinate of the log of the ratio of their amplitude spectra.

$$Q = \frac{-\pi\,\Delta t}{M}, \tag{6}$$

[†]For brevity we have left out the forward and inverse Fourier transforms as well as a Gabor-domain filtering process applied to the windowed reflectivity so that we may concentrate on the conceptual foundations of the POU.

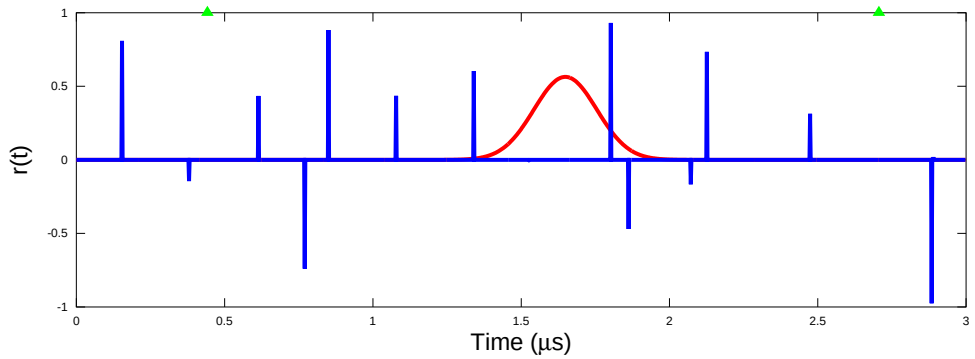

(a)

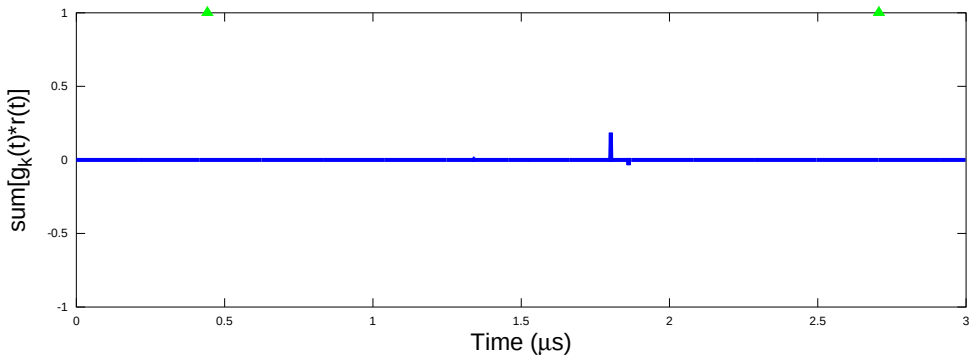

(b)

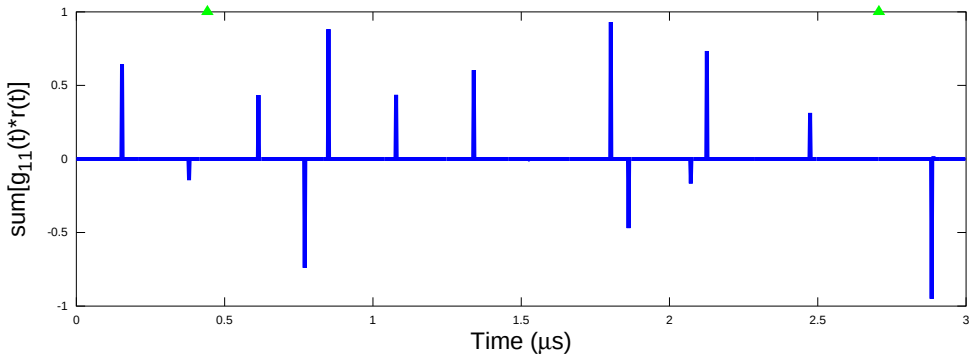

(c)

FIG. 2. Reflectivity example. a) A random reflectivity series. The accurate range of the Gabor transform is indicated by triangles, and the Gaussian highlighted in 1(a) is over-plotted. b) The reflectivity in (a) multiplied by the Gaussian. Reflectivity beyond the range of the Gaussian is set to zero and the *passed* reflectivity is scaled according to the shape of the Gaussian. c) The sum of all 20 windowed reflectivities. Within the accurate range, the reconstruction (inverse Gabor transform) is exactly the same at the original reflectivity in (a).

Parameter	Value
Points in prediction filter	3
Points in Burg spectral estimate	105

Table 1. Parameterization of `burg` (Burg amplitude spectrum estimator) from the CREWES seismic tool box.

where M is the slope of the log-spectral ratio

$$M = \frac{d}{df} \log \left\{ \frac{A_1(f)}{A_2(f)} \right\} \tag{7}$$

The resulting stationary estimate for Q is assumed to be constant for all f (though this is not precisely consistent with equation 5).

Using raw data from Ferguson et al. (2012a) (line 40) the following Q estimation procedure is followed:

1. Compute the mean trace of the data and subtract this trace so that laterally coherent system noise is attenuated .
2. Pick two time windows the same size that spans the range of good signal. The separation between the windows should be 3 times (or more) the size of the windows.
3. Use `burg.m` from the CREWES toolbox to compute the Burg amplitude spectra for the two windows. Burg spectra are more robust than Fourier spectra for small windows Table 1.
4. Input the burg spectra into `sprat.m` from the CREWES toolbox to estimate Q using the spectral ratio method. The `sprat.m` algorithm will compute the log-spectral-ratio (LSR) and plot it versus frequency. Theory suggests that the LSR will be a straight line with negative slope. In practice we find this behaviour over a limited frequency range only.

The Q estimate for our data is shown in Figure 3. As expected, the negative LSR slope is linear between a fixed frequency range between 60 MHz and 220 MHz. This value is consistent with Q values reported by others (Irving and Knight, 2003, for example).

SYNTHETIC EXAMPLES

Forward modelling

Based on the attenuation work of Futterman (1962) we generate a reflectivity series which we then convolve with a minimum phase wavelet. The resulting band limited trace is then transformed into the Gabor (t, f) domain. There, the trace amplitude is multiplied by a real-valued exponential A that attenuates the amplitude

$$A(t, f) = e^{-\pi t f / Q}, \tag{8}$$

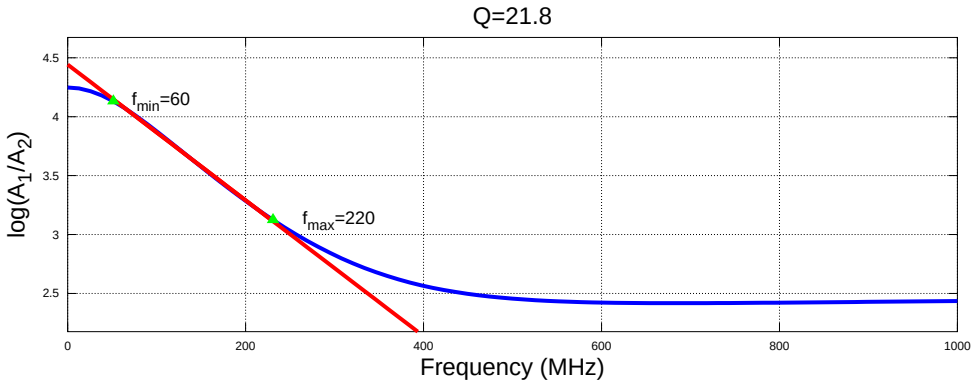

FIG. 3. Q estimate for the data of line 40 (Ferguson et al., 2012a).

where $Q = 21.8$ for georadar and $Q = 218$ for seismic, and then by a complex valued exponential that causes phase dispersion according to

$$B = e^{-i\,H\{-\pi\,t\,f/Q\}}. \tag{9}$$

The results of the above process are given for georadar $(f_{dom} = 200\text{MHz})$ and seismic $(f_{dom} = 20\text{Hz})$ respectively in Figure 4. Not that the reflectivity signals (red curves) are identical with the exception of the different time axes (nano seconds verses seconds), and the bandlimited reflectivities (blue curves) are very similar due to the choice of dominant frequencies. The applied attenuation, however, causes significant differences in the signals (green curves). The seismic signal (Figure 4(a)) is attenuated, but this effect is not strong and the dispersion is not obvious until later times around 0.15 seconds where misalignment of peaks and troughs becomes apparent. By 0.4 seconds, misalignment of zero crossings is evident. Attenuation of the georadar signal (Figure 4(b)) is much stronger and dispersion is evident at 5 ns and increase significantly from there. The attenuated reflection data from 4 are then input to Gabor decon function `gabordecon` from the CREWES toolbox. The results shown in 5 are what we consider to be an optimal balance of input values. The seismic signal (Figure 5(b)) has been phase corrected and gained by Gabor decon such that there is significant overlap with the bandlimited signal at most of the reflection features with some over estimation of amplitude at the later times. The georadar signal (Figure 5(a)) is quite will restored at early times but some fidelity is lost beginning at about 20 ns where amplitudes and trough / peak / zero crossings begin to diverge. Though not a perfect restoration, the signal is still interpretable and therefore very useful in particular when compared with it's original, attenuated and dispersed state (Figure 4(a)).

CONCLUSIONS

We present a theoretical and synthetic development that suggests that Q compensation by Gabor decon (nonstationary deconvolution) is the mechanism by which so many georadar datasets are improved. The attenuation factor Q for georadar is about 10 times smaller and therefore georadar attenuation effects of amplitude decay and phase dispersion are much more pronounced. We find that, for realistic frequencies Gabor decon enhances

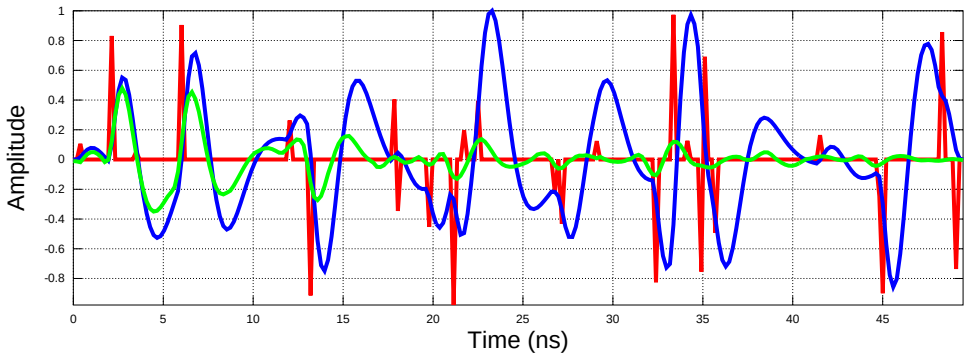

(a)

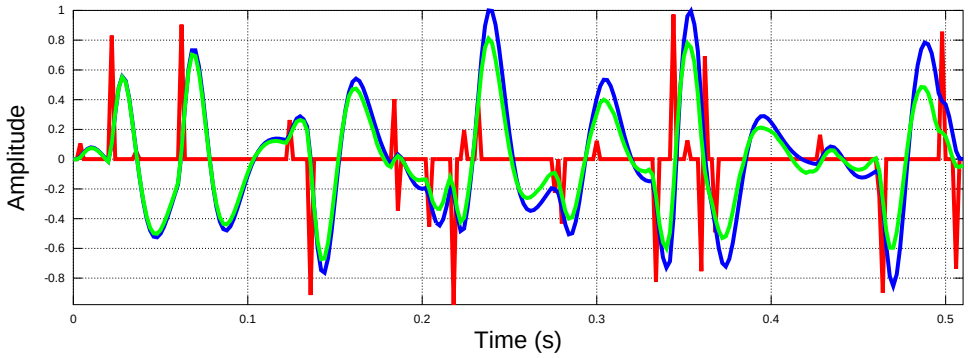

(b)

FIG. 4. Comparison of georadar attenuation (Q=21.8) and seismic attenuation (Q=218) for the same reflectivity series. Figures 4(a) and 4(b) have reflectivity r plotted in red, $r \cdot w$ plotted in blue, and $r \cdot w \cdot \alpha$ plotted in green. a) For $t_{max} = 10^-7$ s, $f_{dom} = 200$ MHz, and $Q = 21.8$, the georadar signal is strongly attenuated (the green curve departs significantly from the blue curve) relative to the seismic signal. b) For $t_{max} = 1$ s, $f_{dom} = 20$ Hz, and $Q = 218$, the seismic signal is not strongly attenuated relative to the georadar signal.

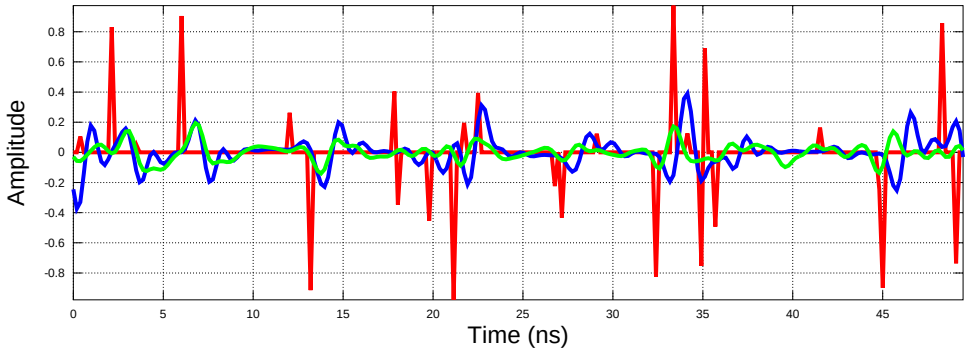

(a)

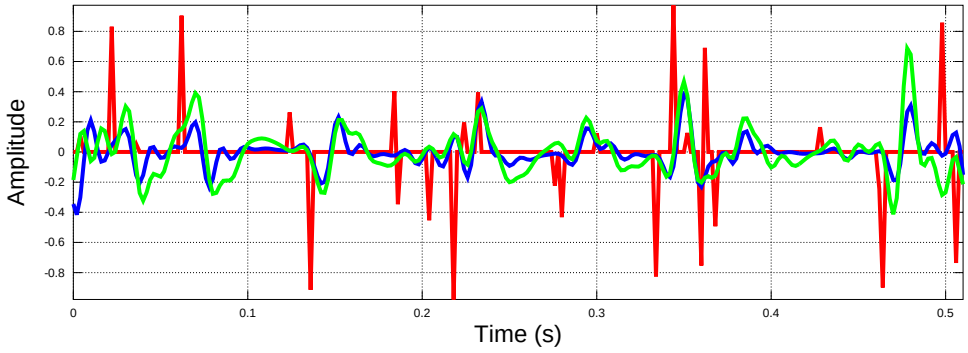

(b)

FIG. 5. Gabor decon applied to the attenuated signals from Figure 4. Green curves are the restored signals. a) The georadar signal is fairly well restored with amplitude and phase departures beginning at about 20 ns. b) The seismic signal is very well restored.

seismic signals as expected and that georadar signals can be even more significantly enhances. The amplitude and phase restoration for georadar are not perfect, of course, but the improved signal presence at later times is significant, and we find that a small amount of phase dispersion and amplitude error remains.

ACKNOWLEDGEMENTS

We wish to thank the staff and sponsors of CREWES for their support. We also thank NSERC for their support of this work through CRD grant CRDPJ 379744-08.

REFERENCES

Båth, M., 1974, Spectral analysis in geophysics, *in* Developments in solid earth geophysics: Elsevier Scientific Publishing Company, Amsterdam.

Ferguson, R. J., M. Ercoli, and A. Frigeri, 2012a, Georadar data processing and imaging: paleoseismicity in the piano di castelluccio basin, central italy: Presented at the , CREWES.

Ferguson, R. J., A. Pidlisecky, and C. Rowell, 2010, Shot record depth migration of georadar data: Presented at the CREWES Research Report, CREWES.

Ferguson, R. J., M. J. Yedlin, and L. Nielsen, 2011, Prestack depth migration of bi-static georadar data: Presented at the , European Geophysical Union.

Ferguson, R. J., M. J. Yedlin, C. Pichot, J. Dauvignac, N. Fortino, and S. Gaffet, 2012b, Depth migration of monostatic and bistatic georadar data: Presented at the , CREWES.

Futterman, W. I., 1962, Dispersive body waves: Journal of Geophysical Research, **73**, 3917–3935.

Irving, J. D., and R. J. Knight, 2003, Removal of wavelet dispersion from ground-penetrating radar data: Geophysics, **68**, 960–970.

Margrave, G. F., M. P. Lamoureux, and D. C. Henley, 2011, Gabor deconvolution: Estimating reflectivity by nonstationary deconvolution of seismic data: Geophysics, **76**, W15–W30.

O'Doherty, R. F., and N. A. Anstey, 1971, Reflections on amplitudes: Geophys. Prosp., **19**, 430–458.

Robinson, E. A., 1967, Predictive decomposition of time series with application to seismic exploration: Geophysics, **32**, 418–484.

Rowell, C., A. Pidlisecky, J. D. Irving, and R. J. Ferguson, 2010, Characterization of lava tubes using ground penetrating radar at craters of the moon national monument, idaho, usa: Presented at the , CREWES.

Zener, C. M., 1948, Elasticity and anelasticity of metals: University of Chicago Press.